Compensating Probe Misplacements in On-Wafer *S*-Parameters Measurements

Robin Schmidt, *Member, IEEE*, Simone Clochiatti, Enes Mutlu, *Student Member, IEEE*, Nils Weimann, *Member, IEEE*, Andrea Ferrero, *Fellow, IEEE*, Michael Dieudonné, and Dominique M. M.-P. Schreurs, *Fellow, IEEE*

***Abstract*— As the maximum frequency of electronics is rising, on-wafer measurements play an important role in modeling of integrated devices. Most of the time, due to the lack of measurement accuracy beyond 110 GHz, such models are usually extracted at frequencies much below their working frequencies and are subsequently extrapolated. The validity of such models is then mostly verified after fabrication of the complete chip, with a simple pass and fail test. This is stating the necessity of enhancing measurement results by any means possible, i.e., to reduce the overall uncertainty in such measurements. It is widely accepted that one of the main sources of uncertainty in such measurements is probe contact repeatability, since it is difficult to reach position accuracy below a few micrometers. We are presenting in this article a method to model the *S*-parameter variation with probe position on the pads, which can then be used to either estimate contact repeatability uncertainty or further enhance measurement results. The approach is validated based on the measurements performed at 500 GHz.**

***Index Terms*— Calibration, on-wafer measurements, probe contact repeatability.**

I. Introduction

ON-WAFER *S*-parameters' measurements have the advantage to characterize on-chip devices without the need for complex waveguide packaging in mm and submm-wave frequencies. In addition, it is a key method for modeling such integrated components, allowing for a much closer evaluation of the manufacturing process, thus improving the overall performance of integrated circuits at these frequencies. The main reason is that the calibration plane is defined directly in the substrate transmission lines. Therefore, it is much closer to the integrated components, without the need to use approximate connector deembedding methods.

Manuscript received 21 April 2022; revised 28 June 2022; accepted 25 July 2022. Date of publication 23 September 2022; date of current version 4 November 2022. This work was supported by the European Union's Horizon 2020 Research and Innovation Program under Marie Skłodowska-Curie Grant 765426 (TeraApps). *(Corresponding author: Robin Schmidt.)*

Robin Schmidt is with Keysight Technologies Inc., 3110 Rotselaar, Belgium, and also with the WaveCoRE Departement, Katholieke Universiteit Leuven (KU Leuven), 3000 Leuven, Belgium (e-mail: robin.schmidt@keysight.com).

Simone Clochiatti, Enes Mutlu, and Nils Weimann are with the Bauelemente der Höchstfrequenz-Elektronik (Components for High-Frequency Electronics), University of Duisburg-Essen, 47057 Duisburg, Germany.

Andrea Ferrero and Michael Dieudonné are with Keysight Technologies Inc., 3110 Rotselaar, Belgium.

Dominique M. M.-P. Schreurs is with the WaveCoRE Departement, Katholieke Universiteit Leuven (KU Leuven), 3000 Leuven, Belgium.

Color versions of one or more figures in this article are available at https://doi.org/10.1109/TMTT.2022.3205606.

Digital Object Identifier 10.1109/TMTT.2022.3205606

The performance of vector network analysis was significantly enhanced in recent years, thanks to the introduction of zero bias Schottky diodes in mixers and multiplier chains' part of the frequency extension modules [1]. In parallel, the probing technology also got further enhanced [2], reaching nowadays up to 1.1 THz, owing to the micromachining process.

Since most calibration algorithms suppose that only one or two modes propagate in the transmission lines, the unshielded environment of on-wafer measurements makes such calibration sensitive to many more uncertainty sources. These include additional unexpected propagating modes [3] and evanescent modes around the probe transition [4]. In addition, any change in the probe behavior between calibration standards and device under test (DUT) will also degrade the measurement accuracy. Such changes may be caused by parasitic coupling to neighboring structures [5], or more obviously, by probe contact variation on the pads making the transition, i.e., probe contact repeatability.

A lot of research has been carried out recently to further improve the accuracy of probe positioning [6] and probe planarity [7], permitting a clear enhancement of measurement accuracy at high frequencies [8]. Automated techniques require a well-calibrated xyz stage and may not be applicable to manual probe stations.

In addition, probe contact repeatability is usually estimated by repeated measurements on various calibration standards [9]. To obtain a statistically valid uncertainty evaluation, at least a dozen of touchdowns are usually necessary. This describes the type *A* approach to evaluate contact repeatability uncertainty [10].

By evaluating the variation in the transition behavior with the probe position, we are aiming to model the systematical part of contact repeatability, composed of the probe mispositioning error. This is not meant to replace the statistical study which is still necessary to understand the random effects, linked to contact resistance, tilt, and probe height variation. As optical microscopes are usually used to visualize the contact, it is possible with simple image processing techniques to obtain the final position on the pads.

In Section II, we first present a method to evaluate the probe transition variation with respect to the probe position on the pads. Then, in Section III, we introduce a calibration algorithm permitting to further enhance the measurement results by compensating the probe position in the measurements. Finally, in Section IV, we present the measurement results when

applying this new method, before discussing its validity in Section V.

II. Model Description

Based on the multiline thru reflect line (TRL) calibration, S-parameters correspond to the traveling wave effectively propagating in the transmission line [11]. Therefore, the S-parameters are normalized to the line impedance, which is *a priori* unknown. Several methods exist to determine the transmission line impedance, either based on the propagation constant and the hypothesis that the capacitance remains constant over the whole frequency band [12], [13] or using model-enforced calibration comparison [14]. While the first method may only be valid in specific cases, the second method heavily relies on well-defined error terms. As a consequence, we would benefit from a general method without the necessity to specify any impedance, i.e., by only using S-parameters.

In [15], we were aiming to model such variation based on lumped elements. While such model requires a known line impedance, it is quite limited to the number of parameters that would need to be fit, easily falling into Occam's razor caveat, and still remains an approximation. Another method described in [16] also proposed the use of a simple stub model based on the line propagation constant and impedance.

The following model only presumes that there is one mode propagating and that the change in transition behavior with the probe position is a local phenomenon. While the unimodality hypothesis is similar for most calibration algorithms, the locality of the phenomena should be verified with a sufficient distance to the calibration plane. From the multiline TRL calibration, we first obtain the following relationship between switch terms' corrected measurements T_{raw}, left/right error boxes T_A/T_B, and calibrated results T_{cal}:

$$T_{\text{raw}} = T_A T_{\text{cal}} T_B. \tag{1}$$

We can then introduce the variation in the transition behavior as two cascade matrices localized at the left/right probe pads R_a/R_b. Using the propagation constant, we can numerically relocate the phenomena by deembedding them from the calibration plane to the pads with L. This permits the reflection components' phases to have a more stable cross-frequency behavior and provides much better agreement with the simulated results. In addition, since no correction was applied yet, T_A and T_B of (1) are only approximating the actual error boxes T'_A and T'_B of the following equation:

$$T_{\text{raw}} = T'_A(L^{-1}R_a L)T_{\text{act}}(L R_b L^{-1})T'_B. \tag{2}$$

A. Estimation of R Matrix

It was demonstrated in [15] that during measurements, it is possible to track down the variation in the transition's S-parameters with respect to the probe position. This can be achieved by letting one of the probes fixed on any line standard, and moving the second probe at various positions p_i. For reference, herein, we chose to move the probe on the right side. By forming (3), the steady term R_a cancels. Under the locality and unimodality assumptions, we can therefore conclude that the exact position of probe port 1 has no influence on the extraction method

$$T_{\text{raw}0}^{-1}T_{\text{raw}i} = T_B'^{-1}L R_{b0}^{-1}R_{bi}L^{-1}T'_B. \tag{3}$$

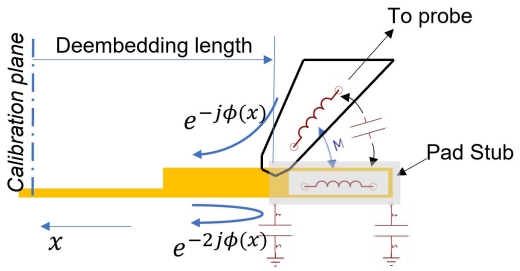

Fig. 1. Simplified probe stub coupling.

The reference position p_0 can be chosen arbitrarily, where we set $R_{b0} = I$. Yet, T'_A and T'_B are not exactly known, and as a consequence, we can only approximate them in the first instance. We can relate the estimates and actual error boxes by the following equation where the position p_c designates the approximate position of the first calibration, and R_{bc} designates the bias introduced in this experiment when $p_0 \neq p_c$:

$$T_B \sim L R_{bc} L^{-1} T'_B \tag{4}$$

$$\begin{aligned} R_{\text{est}i} &= L^{-1}T_B T_{\text{raw}0}^{-1}T_{\text{raw}i}T_B^{-1}L \\ &\sim R_{bc}^{-1}R_{bi}R_{bc}. \end{aligned} \tag{5}$$

While the position p_c is only approximate, we can expect it to be close to the probe position on the Thru line of the initial calibration. Hence, to ensure that $R_{bc} \to I$, a good choice of reference position p_0 is the closest one to the probe position on the Thru.

We now need to interpolate $R_{\text{est}}(x, y)$ with the probe position on the pads. A first method consists of simply imposing reciprocity condition, fixing the number of complex variables to interpolate at three. We can then fit a polynome to the nth order to each of these variables, i.e., $\Delta S_{11}(x, y)$, $\Delta S_{12}(x, y)$, and $\Delta S_{22}(x, y)$.

While this general approach seems to already give good results, it may be useful to further reduce the number of variables to fit by imposing additional conditions to this matrix, to increase its robustness to uncertainty.

B. Lossless Condition

Connector repeatability error is usually represented as a small lossless symmetric perturbation [17]. Thus, retaking our previous formulation, $\Delta S_{11} = \Delta S_{22}$. While this may be true in connectors, it is possible to find a unitary matrix factorization much closer to the actual phenomena of probe movements along the pads, as illustrated in Fig. 1. Such factorization may be written as in the following equation:

$$S_{\text{int}} = \begin{bmatrix} \pm j e^{2j\phi}e^{j\phi_a}\sin(\theta) & e^{j\phi}\cos(\theta) \\ e^{j\phi}\cos(\theta) & \pm j e^{-j\phi_b}\sin(\theta) \end{bmatrix}. \tag{6}$$

With $\phi(x)$, $\theta(x)$, $\phi_a(x)$, and $\phi_b(x)$ being fit parameters according to the position. More specifically, for this matrix, lossless condition additionally enforces $\phi_a = \phi_b$.

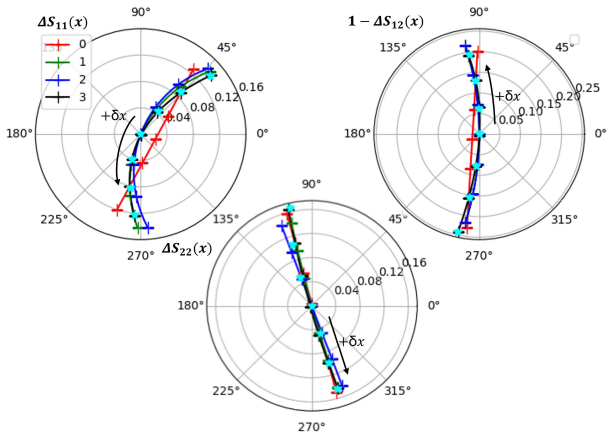

Fig. 2. Simulation results and different interpolation models at 500 GHz, for offset position $\Delta x \in [-12, 12\ \mu\text{m}]$ (0: first-order polynomial model, 1: first-order lossy model, 2: first-order lossless model, 3: second-order polynomial model, and cyan star: simulation results).

The simulation results in Fig. 2 imply that with small displacement, the lossless model is very close to the actual phenomena. Though in the case of significant displacement, to further reduce the interpolation error, it is possible to release this last constraint by considering $\phi_a \neq \phi_b$, introducing our lossy model.

Imposing lossless condition also avoids additional variation with the position of this matrix's transmission. As we will see in Section V, we can observe a dependence of the extracted model to the length of the line standard on which it was extracted on. We believe that this is caused by the nonlocal effects, certainly linked to the parasitic probe effects described in [18] and [4], which mainly affects the transmission coefficients.

C. Extension to Lateral Position

While current factorization may accurately model any displacement along the pads, it can also capture the variation in behavior with lateral movements if they remain lossless. However, slotline (SL) mode is expected to propagate when coplanar waveguide (CPW) grounds are not connected by bridges. In these conditions, the CPW mode may start to weakly couple to SL modes, with lateral mispositions.

The transition itself will then not consist of only a two-port matrix, but most likely of a four-port matrix, linking on both sides the modes propagating in the probe tips and the modes propagating in the transmission lines

$$S_{\text{pb}} = \begin{bmatrix} S_{\text{cpw}} & S_{\text{sl}\to\text{cpw}} \\ S_{\text{cpw}\to\text{sl}} & S_{\text{sl}} \end{bmatrix} \tag{7}$$

$$\begin{aligned} S_{\text{cpw}}(-x) &= S_{\text{cpw}}(x) \\ S_{\text{sl}}(-x) &= S_{\text{sl}}(x) \\ S_{\text{sl}\to\text{cpw}}(-x) &= S_{\text{cpw}\to\text{sl}}(-x) \\ &= -S_{\text{cpw}\to\text{sl}}(x) \\ S_{\text{cpw}\to\text{sl}}(0) &= 0. \end{aligned} \tag{8}$$

Ideally, we can expect the conditions described by (8) on the different 2×2 matrices forming the four-port *S*-parameters. While such relationships can be verified thanks to 3-D full-wave simulations, transmission between CPW and SL modes where expected only to be found below -35 dB in the worst condition, i.e., most forward position, most misaligned. While this may be the case in simulations, it is possible to find probes that certainly couple to the SL modes directly due to introduced asymmetry at the probe tips. This can be explained by various factors, from the most probable to the least: impurities sticking to the probe, probe aging, or even manufacturing inaccuracies.

III. Possible Recalibration Scheme

To find the actual error boxes T'_A and T'_B of (2), we can use a nonlinear least-square fitting method following developments made in [19]. After a first multiline TRL calibration, we already obtain good estimates of the propagation constant, left and right error boxes T_A and T_B, which is useful for the initial conditions of the optimization scheme.

A. Mathematical Approach

The algorithm consists of the minimization of a set of equations constituting the measurement model. Retaking (2) and now that we have an estimate for the displacement function, we are aiming to estimate T'_A and T'_B. The overdetermined set of equations are given by the left and right R-matrix $L_b = (LR_bL^{-1})_{T\to S}$, the different lines defined by their propagation constant (9), and by the reflects only defined by their symmetrical termination as follows:

$$\widehat{S^k_{\text{raw}}}(S_a, S_b, \gamma) = S'_a * L_{ak} * \begin{bmatrix} 0 & e^{-\gamma l_k} \\ e^{-\gamma l_k} & 0 \end{bmatrix} * L_{bk} * S'_b \tag{9}$$

$$\widehat{S^k_{\text{raw}}}(S_a, S_b, \Gamma_{Lk}) = S'_a * L_{ak} * \begin{bmatrix} \Gamma_{Lk} & 0 \\ 0 & \Gamma_{Lk} \end{bmatrix} * L_{bk} * S'_b. \tag{10}$$

Finally, we define the cost function to be minimized as the difference in raw measured and raw estimated *S*-parameters, which are defined by the seven error terms in S'_a and S'_b, propagation constant γ, and the symmetrical reflection coefficients of the reflects Γ_{Lk}

$$r^{ij}_k(S_a, S_b, \gamma, \Gamma_{Lk}, \ldots) = S^{ij}_{\text{raw}} - \widehat{S^{ij}_{\text{raw}}}. \tag{11}$$

Such minimization problem is then solved using the Levenberg–Marquardt (LM) algorithm. This is completed with eight cores in 58 s for 200 frequency points. In comparison, more classical minimization techniques approximately perform five times slower.

In Appendix A, we also developed equations that include repeatability correction to the general Thru-circuit-unknown (TCX) algorithm from [20]. The derivation in terms of *S*-parameters helps greatly to include our new terms to the first order. In comparison, this last algorithm only takes 10 s on a single core to be solved while giving similar results.

Finally, once the new error terms are found, by knowing the position of the probes during the DUT measurement, we can simply apply the inverse of the relationship (2), which leads to the following equation:

$$T_{\text{act}} = \left(L^{-1}R_a^{-1}(x_a)L\right)T_A'^{-1}T_{\text{raw}}T_B'^{-1}\left(LR_b^{-1}(x_b)L^{-1}\right). \tag{12}$$

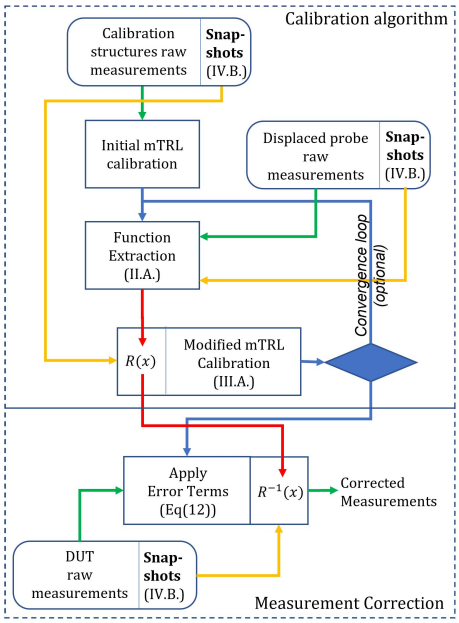

Fig. 3. Summary of the calibration algorithm (yellow arrows: probe positions, green arrows: measurement data, blue arrows: error terms, and red arrows: displacement function).

The diagram of Fig. 3 describes the global behavior of the proposed calibration algorithm, where we represented the different fluxes of information necessary to its completion.

B. Residuals Definition and Uncertainty

To verify the validity of the approach, we first need to introduce few definitions since classical calibration comparison to the multiline TRL will only give a rough idea of the gain in accuracy.

As pointed out in [19], the main advantage of the LM minimization technique is that we can easily obtain a good estimate of the error terms' covariance matrix, based on the calibration residuals r_k^{ij}, the sensitivity of the objective function to each parameter $J^T J$ with J being the Jacobian matrix at the minimum, and the naive statistical degree of freedom $n-m$, with n the number of observations, and m the number of parameters. For clarification, each line gives four observations, while each reflect only gives two

$$\text{cov}(\beta) \sim \frac{\sum |r_k^{ij}|^2}{n-m} * (J^T J)^{-1}. \tag{13}$$

Using this first definition, we can finally obtain the error terms of the calibration with their uncertainty. With this covariance matrix, we can easily propagate error terms' uncertainty into the calibrated DUT S-parameters using the Monte Carlo simulation. However, to obtain comparable results in terms of propagated uncertainty, we will have to distinguish repeatability uncertainty in case 1, when we do not apply mispositioning compensation, and in case 2 when applying the full compensation algorithm.

In case 1, to include repeatability uncertainty to the uncompensated results, we have to remind that the current R-matrix was extracted with reference to T_B'. Thus, it is necessary to compensate for the shift of reference plane between T_B and T_B'. We relate the R-matrix of case 1 R_b to the R-matrix of case 2 R_b' by supposing that the reference position in case 1 corresponds to the mean of the distributions δx of Fig. 7

$$L R_b(\delta x - \overline{\delta x}) L^{-1} T_B \sim L R_b'(\delta x) L^{-1} T_B'. \tag{14}$$

We can then reuse (4) to obtain the actual repeatability function in case 1

$$R_b(\delta x - \overline{\delta x}) \sim R_b'(\delta x) R_b'^{-1}(\overline{\delta x}). \tag{15}$$

Finally, mispositioning uncertainty is propagated by injecting distributions in the R-matrix and form the following equation:

$$\delta T_{\text{cal}} = L^{-1} R_a(\delta x_a - \overline{\delta x_a}) L T_{\text{cal}} L R_b(\delta x_b - \overline{\delta x_b}) L^{-1}. \tag{16}$$

In case 2, we would require a more complete study to model the uncertainty of the displacement function. A possible type A approach to the evaluation of the random part of probe contact repeatability is to perform the complete cycle of "calibration–function extraction–compensation" several times. Through the variation in the extracted function and the compensated results, we would consequently obtain an estimate of the uncertainties caused by the function and by the random part of contact repeatability. However, since we did not perform such measurements, we only considered the position indeterminacy linked to the microscope resolution, at around 0.5 μm. Similar to case 1, position indeterminacy is propagated using (16).

Another method, which does not require to define the uncertainty of the extracted function, is to compare the overall residuals of the LM calibration in both the cases. For the TCX approach, we used the same residuals' definition as in (11). The final residuals for both the cases in the LM and TCX calibrations can be found in Fig. 4, where we clearly observe a reduction in overall residuals when applying the correction.

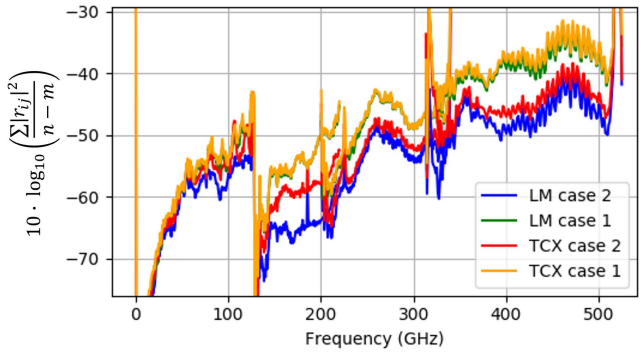

Fig. 4. Sum of squared residuals.

IV. Measurements

A. Setup

The measurement setup consisted of a CM300x probe station (FormFactor) and two RPP504 xyz stages for the probe positioners. To reduce the drift impact on the measurements, very short 45° sections of waveguide were used to connect the probes to the Virginia Diodes' frequency extenders, themselves placed at 45° on Formfactor's mini extender arms. The network analyzer and the probe station were controlled via python scripts running on a laptop. For measurements in the WR3.4 and WR2.2 bands, 50-μm pitch Dominion MicroProbe

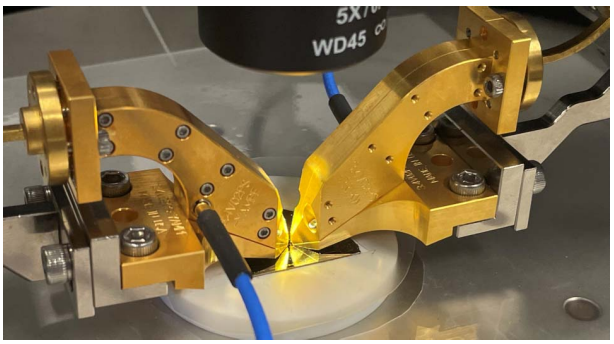

Fig. 5. 330-GHz DMPI probes measuring on ceramic chuck.

Inc. (DMPI) microfabricated probes suited our evaporated gold pad surfaces. WR2.2 probes were in a very good state, while WR3.4 probes seemed already a bit worn out. For the single sweep up to 220 GHz, measurements were performed on the new broadband vector network analyzer (VNA) solution from [21]. The crossover region between the Coax and WR5.1 waveguide band not being optimized yet at the time of the measurements, the spike visible around 130 GHz was caused by a significant loss of directivity. To avoid the propagation of parasitic modes, the measured substrate was placed on a 5 mm ceramic chuck with a relative permittivity of 14, as shown in Fig. 5.

It is important to specify that the setup was regularly mounted and dismounted, and the positioner axes were compensated using our own algorithms while the probe position was considered as steady. Unfortunately, due to limited time, we could not fully identify why the probe position was slightly drifting, even after long warm-up time. Several external sources of drifts can be the cause of such variation, including small variation in room temperature, where the probe position can have a dependence of several μm/°C. This justifies Formfactor's automatic positioning algorithms (Contact Intelligence) that we, however, did not use during these measurements. As a result, we could only reach position accuracy of ± 3 μm, which could have been reduced under ± 1 μm with Contact Intelligence.

B. Position Detection

During each measurement, a snapshot from both the landed probes was taken. Based on these pictures, it was possible to use simple image processing techniques to find the relative positions of the probes with respect to the signal launchers. We first performed a bilinear interpolation to numerically augment the number of pixels, thus enhancing the accuracy of the detection below microscope pixel level. Then, to reduce the influence of the signal launcher structure on the detected probe position, we used different masks by filtering the image based on color ranges.

Finding the optimal position consisted of minimizing a cost function composed of the differences between the positioned feature and the corresponding mask. Since we did not require too much speed in postprocessing, we simply went through all the possible positions within a rectangle approximately enclosing the final position. An example of the output can be found in Fig. 6.

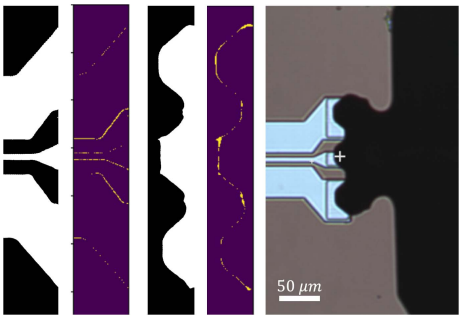

Fig. 6. Left to right: filtered launcher, differences at position, filtered probe tip, differences at position, and found positions.

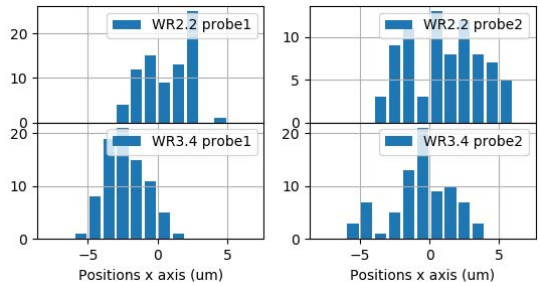

Fig. 7. Detected position histograms (variation probably caused by room temperature).

C. Calibration Substrate

We designed an extended multiline TRL set that was implemented with evaporated gold on a 400-μm-thick indium phosphide (InP) substrate. The CPW transmission line has dimensions of 6-μm signal linewidth, 5-μm gap, and 90-μm total width. The total width was chosen to avoid the additional radiation effects at high frequencies [22]. The signal and gap sizes were chosen based on the manufacturing constraints, while respecting the conclusions made in [4], i.e., $W_{\text{gnd}} \geq 2W_{\text{gap}} + W_{\text{sig}}$. Finally, the pads and tapers were designed to permit the use of various 50-μm pitch probes on such narrow coplanar structures. The size of the signal pad was set to 18 per 30 μm permitting a significant probe skating in case of tip planarity issues.

The calibration set consisted of 12 lines going from a very short Thru of only 180-μm length to a long line of 2484 μm, as well as offset reflects of various lengths. Next to this, we also implemented several verification structures mainly composed of mismatched lines of various lengths. Following the guidelines of [5], a significant spacing was used to avoid coupling to neighboring structures, thus using 750 μm of lateral spacing and 900 μm of longitudinal spacing.

Table I describes the dimensions of some of the structures, which includes uncertainty caused by substrate's inhomogeneity, where W_{gap} designates the gap width, W_{tot} is the total width, W_{sig} is the signal conductor width, T_{cond} is the thickness of the conductors, L_{tot} is the total length from edge to edge, and L_{eff} is the effective length from the initial calibration plane. These values were determined by characterizing the topology of several structures across the wafer with a confocal microscope. It is still unclear at this point whether the obtained uncertainty values are inherent to the measurement methodology or to actual wafer inhomogeneity.

TABLE I
DIMENSIONS IN μm OF SOME CALIBRATION AND VERIFICATION STANDARDS

Name	W_{gap}	W_{tot}	W_{sig}	T_{cond}	L_{tot}	L_{eff}
Thru	$4.99 \pm .17$	$89.63 \pm .13$	$5.91 \pm .16$	$.395 \pm .015$	180	0
Line36	$4.99 \pm .17$	$89.63 \pm .13$	$5.91 \pm .16$	$.395 \pm .015$	216	36
Line108	$4.99 \pm .17$	$89.63 \pm .13$	$5.91 \pm .16$	$.395 \pm .015$	288	108
Line180	$4.99 \pm .17$	$89.63 \pm .13$	$5.91 \pm .16$	$.395 \pm .015$	360	180
Line2304	$4.99 \pm .17$	$89.63 \pm .13$	$5.91 \pm .16$	$.395 \pm .015$	2484	2304
Shorts144	$4.99 \pm .17$	$89.63 \pm .13$	$5.91 \pm .16$	$.395 \pm .015$	85.5	-16
Opens216	$4.99 \pm .17$	$89.63 \pm .13$	$5.91 \pm .16$	$.395 \pm .015$	121.5	16
Beatty	~ 8.5	$90.1 \pm .34$	~ 3.0	$.395 \pm .015$	756	576

D. Crosstalk Effects and Anomalies

The use of shorter lines serves the verification of nonlocal effects when extracting the repeatability model and permits to visualize anomalies in short CPW transmission lines as discussed in [18]. Thus, after several trials, the shortest line effectively used as a Thru was the one of 258 μm, i.e., "Line108" by following our notation. We plotted the calibrated line transmission in Fig. 8, where we can clearly observe the aforementioned anomalies. Interestingly, unlike the Multical implementation of the mTRL algorithm, both the LM and TCX approaches do not assume the chosen Thru as being perfect.

Comparatively, we also measured similar structures with air bridges to understand whether such effects could be associated with SL mode propagation, but such phenomenon was sensibly similar. On the contrary, on the lower portion of the WR3.4 waveguide band, we were able to identify a significant injection of SL modes when measuring open standards with the probe on port 1, which mainly had an influence on the computation of the symmetry factor k (described in Appendix).

Astonishingly, even the 756-μm-long line is experiencing a similar behavior. The fact that such phenomenon is present at $k \times f_c$ frequencies with k an integer may suggest that it is coming from some resonant mode. In fact, the probe tips of $\approx$400 μm are reaching one wavelength at frequencies around 250 GHz, thus giving maximum radiation efficiency. In Fig. 8, we were effectively able to measure a significant transmission of more than -30 dB in various reflects' standards. Isolation of such structures being normally much lower, their transmission is quite representative of the magnitude of probe crosstalk effects. We can clearly observe the correlation between crosstalk magnitude on the reflects' transmission and frequencies at which anomalies occur. This strongly suggests that probe crosstalk is at least partially responsible for such anomalies.

E. Results

Initially, after performing a multiline TRL calibration, we directly extracted the displacement model on several transmission lines using the method described in Section II.

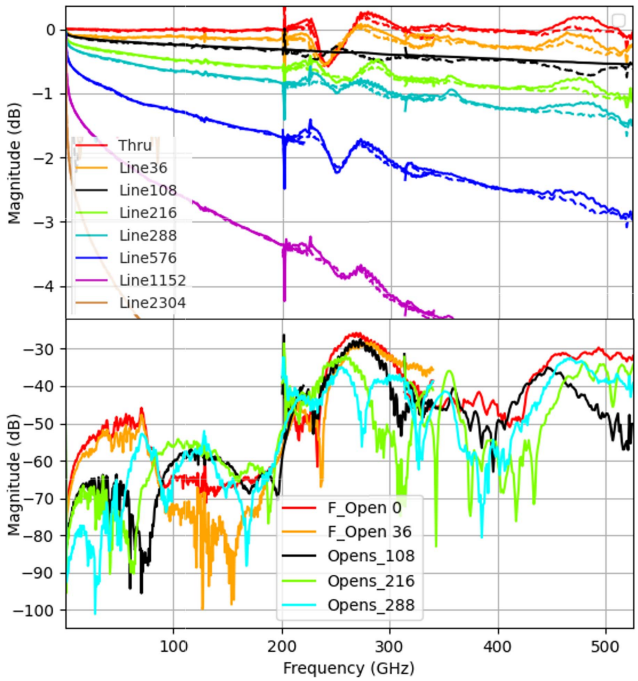

Fig. 8. Top: calibrated lines' transmission (continuous: NIST MultiCal mTRL and dashed: optimal mTRL). Line108 was used as the Thru in the calibrations. Bottom: transmission of open standards using similar probe separation.

A first verification of the model validity was then performed by compensating measurements of various reflects' standards when the probe was voluntarily displaced on the pads (not shown here). While this seemed to give satisfying results on each individual standard by significantly reducing the S-parameters' variation, we could not see any enhancement in the behavior of extracted lumped element models of similar standards with various offset lengths. Such unsatisfactory results are explained by the undefined calibrated position p_c in (4), i.e., by the approximate error terms of the initial calibration T_A and T_B. This yielded our new approach to the calibration, permitting to properly define error terms and reference positions.

To demonstrate the output of different calibration algorithms, we plotted in Fig. 9 the calibrated results of a mismatched line in which reflection coefficients are quite sensitive to probe displacements. In addition, in Fig. 10 we plotted the calibrated results of an offset serial load after moving the calibration plane to its center. These results clearly demonstrate an enhancement in terms of continuity between waveguide bands and reduce the discrepancies caused by inaccurate probe positioning. Finally, we can observe that the TCX algorithm results are very close to the LM approach in both the cases.

The error bars were computed based on the Monte Carlo simulations by only considering high- and low-level noises, calibration residuals, mispositioning in case 1, and position indeterminacy in case 2. Noises were considered uncorrelated from the other uncertainty sources. From (13), we obtained estimates of the error term covariance matrix based on the residuals, which could be directly used in a multivariate normal distribution. Finally, the random position obtained

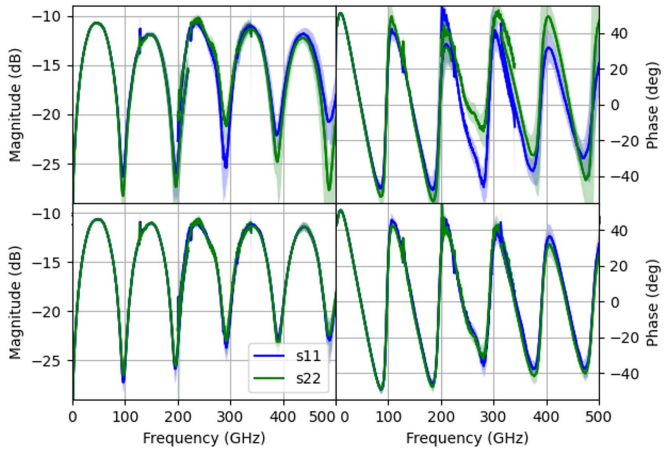

Fig. 9. Calibration verification on Beatty lines. (Top: uncorrected LM with uncertainty bounds ($k = 2$) and bottom: R-corrected LM with uncertainty bounds.)

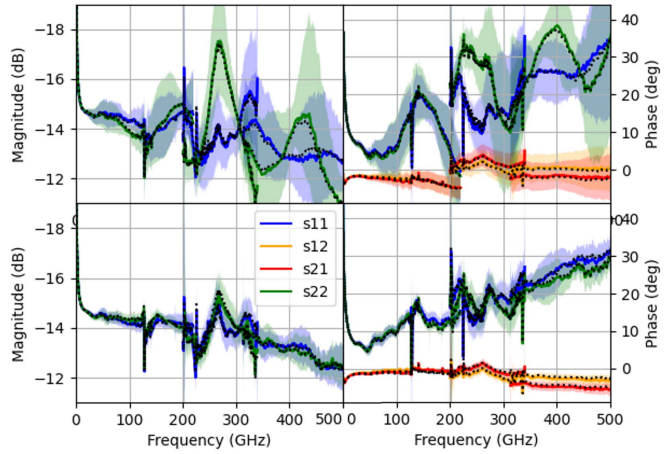

Fig. 10. Calibration verification on deembedded offset serial load. (Top: uncorrected LM with uncertainty bounds ($k = 2$), bottom: R-corrected LM with uncertainty bounds, and black dotted: TCX algorithm output.)

from the distributions of Fig. 7 in case 1, or from position indeterminacy in case 2, can be fed to the extracted displacement function, which consequently keeps the correlations between its output *S*-parameters. Table II summarizes the contribution of each considered sources to the computed error bars. In case 2, we computed the values for position indeterminacy of ± 0.5 and ± 1 μm. Yet, some important contributions are still missing, such as drifts, the random part of probe contact repeatability, and wafer inhomogeneity.

Finally, in Fig. 11, we are comparing the displacement function obtained from the measurements and from 3-D full-wave simulations (Keysight EMpro). The simulation results were obtained with an approximate probe EM model obtained from [16] that we updated based on microscope snapshots of the probes. All the probe materials were taken as lossless to reduce the differences in behavior between simulations. The results are astonishingly close to the measurements, proving that such set of simulations could reproduce the phenomena occurring in the measurements. This gives us an additional tool for the design of signal launchers less sensitive to probe displacements.

TABLE II
PARTIAL UNCERTAINTY BUDGET ON BEATTY LINE

Case 1	55 GHz		239 GHz				490 GHz			
Type	S_{11}	S_{22}	S_{11}	S_{12}	S_{21}	S_{22}	S_{11}	S_{12}	S_{21}	S_{22}
Noises	9.1e-5	9.6e-5	.0049	.0049	.0053	.0053	.0036	.0035	.0024	.0023
Residuals	.0050	.0051	.0110	.0105	.0122	.0107	.0139	.0125	.0108	.0084
Mispositioning	.0034	.0029	.0090	.0134	.0134	.0086	.0250	.0328	.0328	.0315
Combined	.0060	.0060	.0150	.0180	.0189	.0150	.0281	.0341	.0346	.0319
Case 2 $\pm.5$ μm	55 GHz		239 GHz				490 GHz			
Residuals	.0045	.0044	.0076	.0079	.0085	.0072	.0077	.0073	.0063	.0053
Indeterminacy	.0004	.0004	.0050	.0048	.0048	.0050	.0073	.0082	.0082	.0074
Combined	.0042	.0044	.0105	.0099	.0109	.0103	.0130	.0109	.0107	.0093
Case 2 ± 1 μm	55 GHz		239 GHz				490 GHz			
Indeterminacy	.0008	.0008	.0101	.0095	.0095	.0100	.0146	.0163	.0164	.0149
Combined	.0042	.0045	.0142	.0129	.0139	.0133	.0186	.0178	.0179	.0162

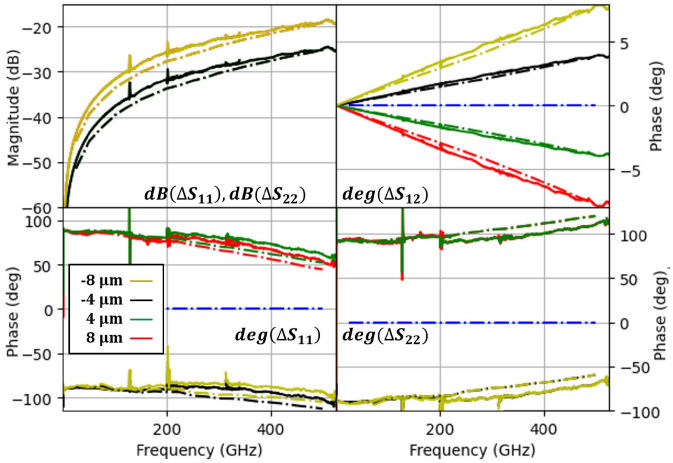

Fig. 11. Model simulated versus extracted on Line216 (continuous: extracted based on measurements and dashdotted: extracted with simulations).

V. LIMITATIONS

When extracting the R-matrix on lines of different lengths using the method presented in Section II, we were able to identify a strong dependency of its terms with the line length, as observed in Fig. 12. In fact, on short lines, the locality hypothesis on which we base ourselves will be invalidated by the presence of evanescent modes and probe crosstalk, as the transitions are closer to each other. The fact that our displacement function is able to capture these effects is suggesting that the anomalies described in [18] are also probe-position-dependent. On excessively short lines, e.g., Thru and Line72 in our case, even the angles of the different terms are affected. The former suggests that the method presented here requires sufficiently long lines to respect the locality hypothesis.

Yet, even under these conditions, concerning Line216, the variation in transmission magnitude with the probe position shown in Fig. 13 is still difficult to capture accurately. In fact, it is first subjected to the anomalies mainly affecting the

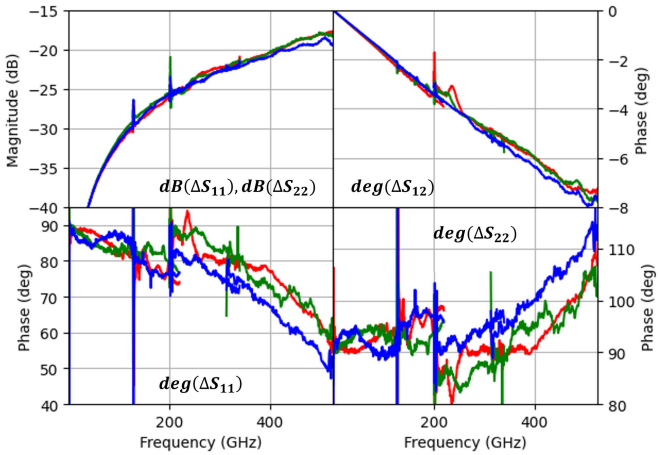

Fig. 12. Displacement of $\Delta x = -8$ μm extracted on lines (red: Thru, green: Line72, and blue: Line216).

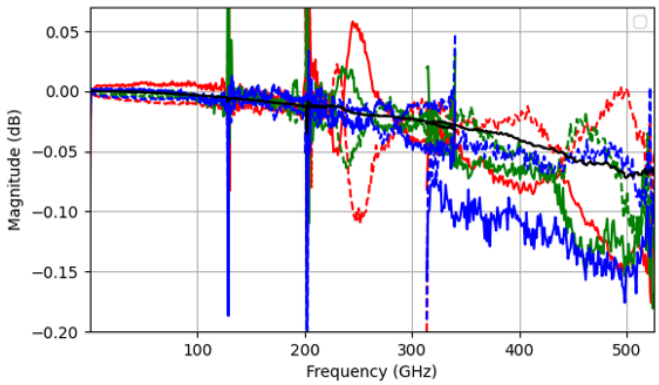

Fig. 13. R-matrix transmission magnitude for $\Delta x = -8$ μm (continuous) and $\Delta x = 8$ μm (dashed) extracted on lines (red: Thru, green: Line72, orange: Line144, blue: Line216, and black: lossless model).

transmission of lines, and to the random contact resistance. Thus, it is preferable to let the lossless model transmission only depend on the R-matrix reflection terms, i.e., $\theta(x)$ is estimated based on the reflection terms.

The current extraction method also relies on one measurement at the reference position, e.g., on T_{raw0} of (5). As a consequence, any error introduced in this unique measurement will then be propagated in the model itself. After a clarification of the uncertainty sources affecting this measurement, we would then benefit from a probabilistic approach to the estimation of such function. Main random effects that are expected to have a significant impact on the extraction of the function are probe height, nonlocal effects, and test fixture drifts.

Finally, as it was the case in the lower portion of the WR3.4 waveguide band, SL mode propagation also impacted this method, thus reducing the enhancement of error terms' definition.

VI. Conclusion

In this article, we successfully developed a new approach to evaluate probe mispositioning effects in on-wafer S-parameters' measurements. After studying the properties of the extracted matrix with accurate 3-D full-wave simulations, we were able to develop a model that does not require the definition of impedance or propagation constant at pad level. Thanks to the generality of the approach, with only small modifications, we expect such model to be applicable to a quite extensive variety of signal launchers.

Furthermore, we demonstrated a possible application of this model by compensating probe misplacement in measurements performed up to 500 GHz. While measurements yielded very promising results by compensating measurement errors introduced by quite significant positioning error of ± 3 μm, the method still requires a deeper uncertainty study to understand how far measurements could be enhanced.

Appendix
Alternative Calibration Algorithm

Based on the calibration algorithm described in [20], it is possible to introduce the terms on the left and right displacement matrices R_a and R_b. To simplify calculus, we used the following notation: $L_{aij} = ((L^{-1}R_aL)_{T\to S})_{ji}$ and $L_{bij} = ((LR_bL^{-1})_{T\to S})_{ij}$.

By following the signal flow charts when adding the displacement matrix on each side of an ideal line, it is first possible to obtain the following system, where A corresponds to the S-parameters of a displacement corrected ideal line:

$$\begin{aligned} A_{11} &= L_{a11} + L_{a12}^2 S_{12}^2 L_{b22} + o(L_{kii}L_{kjj}) \\ A_{22} &= L_{b11} + L_{b12}^2 S_{12}^2 L_{a22} + o(L_{kii}L_{kjj}) \\ A_{12} &= A_{21} \\ &= L_{a12}L_{b12}S_{12} + o(L_{kii}L_{kjj}). \end{aligned} \tag{17}$$

A. Computation of Line Transmission

The following equation is equivalent to the eigenvalue problem from mTRL calibration, thus falling in the same singularity when the angle of the transmission between the Thru and the Line standards are within $\pm k\pi$:

$$\begin{aligned} &M_{A12}M_{B21}\left(R_{a12}^A R_{b12}^A\right)^2 e^{-2\gamma l_A} \\ &\quad + M_{A21}M_{B12}\left(R_{a12}^B R_{b12}^B\right)^2 e^{-2\gamma l_B} \\ &= -(\Delta M_A + \Delta M_B - M_{A11}M_{B22} - M_{B11}M_{A22}) \\ &\quad * e^{-\gamma l_B} e^{-\gamma l_A} R_{a12}^A R_{b12}^A R_{a12}^B R_{b12}^B + o(L_{kii}L_{kjj}) \end{aligned} \tag{18}$$

where M_A and M_B correspond to the raw measured S-parameters of lines of length l_a and l_b after switch terms' correction, respectively, and ΔM_a and ΔM_b their determinant. Manipulations similar than in the mTRL algorithm of [23] can be realized for choosing the correct root and obtaining the weighted least-square solution.

B. Error Terms Computation

To compute the first error terms, we deviate from the multiline TRL algorithm by correcting each of the lines. In fact, the eigenvalue problem on which this algorithm is based is this time ill-conditioned due to the mispositioning of the probes. Recognizing that the ideal lines are corrected by the repeatability function, cascade matrices cannot be considered as diagonal anymore.

Thanks to the expressions clearly derived in [20], a much simpler formulation for our lines can be found based on the *S*-parameters. Equations [20, eqs. (1)–(4)] can be reimplemented, this time using the corrected expressions (17) for each of the ideal lines. The propagation constant having been already calculated in the previous part, we can consider each line to be fully known. We can then simply use $S_{12} = e^{-\gamma l_k}$.

Hence, this forms an overdetermined set of equations, and a least-square solution is found describing error boxes' ports 1 and 2 apart from the well-known symmetry factor. This set of equations benefits from being much less sensitive to errors than the expressions used in the original mTRL algorithm.

C. Symmetry Factor

The next step consists of solving the last symmetry factor, and this is where expressions had to be the most readapted. By considering that errors in reflection are sufficiently low, we can safely use the first-order expressions of (19), where C designates the *S*-parameters of a displacement corrected ideal symmetrical reflect

$$\begin{aligned} C_{11} &= L_{a11} + L_{a12}^2\Gamma[1 + L_{a22}\Gamma + o(L_{kii}L_{kjj})] \\ C_{22} &= L_{b11} + L_{b12}^2\Gamma[1 + L_{b22}\Gamma + o(L_{kii}L_{kjj})] \\ C_{12} &= C_{21} \\ &= L_{a12}L_{b12}T[1 + o(L_{kii}L_{kjj})] \end{aligned} \tag{19}$$

$$N'\underline{E} = G + kH - \Gamma^2(\Delta G + k\Delta H) \tag{25}$$

$$\underline{E} = [\Gamma, k\Gamma, T, kT]^T \tag{26}$$

To solve the system (20)–(26), an additional step compared with the original article has to be followed. First, we can solve the linear part of the equation using least-square method for both $k = 0$ and 1, giving, respectively, $\underline{U}$ and $\underline{W}$ vectors as solutions for $\underline{E}(k = 0)$ and $\underline{E}(k = 1)$. Introducing $\underline{V} = \underline{U} - \underline{W}$, we can obtain a first estimate of Γ using (27). Root choice is made based on the previously declared offset lengths and approximate values for the different reflect standards, e.g., $\min(|1 - \text{roots}(P(\Gamma))/\,\Gamma_{\text{est}}e^{-2\gamma l_{\text{ofs}}}|)$

$$P(\Gamma) = \Gamma^2 - (u_1 + v_2)\Gamma + u_1v_2 - v_1u_2. \tag{27}$$

Once a valid estimate is found for Γ, we can modify the second part of (25) where we use this last estimate to correct G and H using (28). Since both $\Delta G, \Delta H \ll \underline{1}$, the final solution converges in very few loops

$$\begin{aligned} G_{n+1} &= G_0 - \Gamma_n^2\Delta G_n \\ H_{n+1} &= H_0 - \Gamma_n^2\Delta H_n. \end{aligned} \tag{28}$$

Provided that a more close solution is found to estimate T'_A and T'_B, it is possible to further refine the estimate of the repeatability function, thus ensuring that $R_{bc} \to I$ in (5). Again here, due to the same reason, the final solution converges in few loops.

ACKNOWLEDGMENT

The authors especially wish to thank Gavin Fisher (Formfactor) for his help in setting up the probe station and Virginia Diodes Inc. (VDI) for the frequency extender heads.

$$G = \begin{bmatrix} M_{C11} - L_{a11}(M_{C11}x_2 - x_3) - x_1 \\ -L_{b11}M_{C12}x_5 \\ M_{C21} - L_{a11}M_{C21}x_2 \\ -L_{b11}(M_{C22}x_5 - x_6) - x_4 \end{bmatrix} \tag{20}$$

$$H = \begin{bmatrix} -L_{a11}(M_{C11}y_2 - y_3) - y_1 \\ M_{C12} - L_{b11}M_{C12}y_5 \\ -L_{a11}M_{C21}y_2 \\ M_{C22} - L_{b11}(M_{C22}y_5 - y_6) - y_4 \end{bmatrix} \tag{21}$$

$$\Delta G = \begin{bmatrix} L_{a12}^2L_{a22}(M_{C11}x_2 - x_3) \\ L_{b12}^2L_{b22}M_{C12}x_5 \\ L_{a12}^2L_{a22}M_{C21}x_2 \\ L_{b12}^2L_{b22}(M_{C22}x_5 - x_6) \end{bmatrix} \tag{22}$$

$$\Delta H = \begin{bmatrix} L_{a12}^2L_{a22}(M_{C11}y_2 - y_3) \\ L_{b12}^2L_{b22}M_{C12}y_5 \\ L_{a12}^2L_{a22}M_{C21}y_2 \\ L_{b12}^2L_{b22}(M_{C22}y_5 - y_6) \end{bmatrix} \tag{23}$$

$$N' = \begin{bmatrix} L_{a12}^2(M_{C11}x_2 - x_3) & L_{a12}^2(M_{C11}y_2 - y_3) & M_{C12}L_{a12}L_{b12}x_5 & M_{C12}L_{a12}L_{b12}y_5 \\ L_{b12}^2M_{C12}x_5 & L_{b12}^2M_{C12}y_5 & L_{a12}L_{b12}(M_{C11}x_2 - x_3) & L_{a12}L_{b12}(M_{C11}y_2 - y_3) \\ L_{a12}^2M_{C21}x_2 & L_{a12}^2M_{C21}y_2 & L_{a12}L_{b12}(M_{C22}x_5 - x_6) & L_{a12}L_{b12}(M_{C22}y_5 - y_6) \\ L_{b12}^2(M_{C22}x_5 - x_6) & L_{b12}^2(M_{C22}y_5 - y_6) & M_{C21}L_{a12}L_{b12}x_2 & M_{C21}L_{a12}L_{b12}y_2 \end{bmatrix} \tag{24}$$

REFERENCES

[1] T. W. Crowe, J. L. Hesler, E. Bryerton, and S. A. Retzloff, "Terahertz sources and receivers for science applications and test & measurement systems," in *Proc. IEEE Compound Semiconductor Integr. Circuit Symp. (CSICS)*, Oct. 2016, pp. 1–4.

[2] A. Rumiantsev and R. Doerner, "RF probe technology: History and selected topics," *IEEE Microw. Mag.*, vol. 14, no. 7, pp. 46–58, Nov. 2013.

[3] F. J. Schmückle, R. Doerner, G. N. Phung, W. Heinrich, D. Williams, and U. Arz, "Radiation, multimode propagation, and substrate modes in W-band CPW calibrations," in *Proc. IEEE 41st Eur. Microw. Conf.*, Oct. 2011, pp. 297–300.

[4] G. N. Phung and U. Arz, "Parasitic probe effects in measurements of coplanar waveguides with narrow ground width," in *Proc. IEEE 24th Workshop Signal Power Integrity (SPI)*, May 2020, pp. 1–4.

[5] G. N. Phung, F. J. Schmuckle, R. Doerner, T. Fritzsch, and W. Heinrich, "Impact of parasitic coupling on multiline TRL calibration," in *Proc. 47th Eur. Microw. Conf. (EuMC)*, Oct. 2017, pp. 835–838.

[6] R. Sakamaki and M. Horibe, "Accuracy improvement of on-wafer measurement at millimeter-wave frequency by a full-automatic RF probe-tip alignment technique," in *Proc. 91st ARFTG Microw. Meas. Conf. (ARFTG)*, Jun. 2018, pp. 1–4.

[7] R. Sakamaki and M. Horibe, "Proposal of a precision probe-tilt adjustment with the RF signal detection technique," in *Proc. Conf. Precis. Electromagn. Meas. (CPEM)*, Jul. 2018, pp. 1–2.

[8] R. Sakamaki and M. Horibe, "Improvement of on-wafer measurement accuracy with RF signal detection technique at millimetre-wave frequencies," *IET Microw., Antennas Propag.*, vol. 11, no. 13, pp. 1892–1897, Sep. 2017.

[9] U. Arz, S. Zinal, T. Probst, G. Hechtfischer, F. J. Schmückle, and W. Heinrich, "Establishing traceability for on-wafer S-parameter measurements of membrane technology devices up to 110 GHz," in *Proc. 90th ARFTG Microw. Meas. Symp.*, Nov. 2017, pp. 1–4.

[10] *Evaluation of Measurement Data-Guide to the Expression of Uncertainty in Measurement*, Joint Committee for Guides in Metrology, International Organization for Standardization, Geneva, Switzerland, 2008, p. 134, vol. 50.

[11] D. Williams, "Traveling waves and power waves: Building a solid foundation for microwave circuit theory," *IEEE Microw. Mag.*, vol. 14, no. 7, pp. 38–45, Nov. 2013.

[12] R. B. Marks and D. F. Williams, "Characteristic impedance determination using propagation constant measurement," *IEEE Microw. Guided Wave Lett.*, vol. 1, no. 6, pp. 141–143, Jun. 1991.

[13] D. F. Williams and R. B. Marks, "Transmission line capacitance measurement," *IEEE Microw. Guided Wave Lett.*, vol. 1, no. 9, pp. 243–245, Sep. 1991.

[14] S. Amakawa *et al.*, "Causal characteristic impedance determination using calibration comparison and propagation constant," in *Proc. 92nd ARFTG Microw. Meas. Conf. (ARFTG)*, Jan. 2019, pp. 1–6.

[15] R. Schmidt, D. Schreurs, M. Dieudonne, and P. Barmuta, "Model of probe transition including probe mispositioning," in *Proc. 95th ARFTG Microw. Meas. Conf. (ARFTG)*, Aug. 2020, pp. 1–3.

[16] L. Chen *et al.*, "Terahertz micromachined on-wafer probes: Repeatability and reliability," *IEEE Trans. Microw. Theory Techn.*, vol. 60, no. 9, pp. 2894–2902, Sep. 2012.

[17] M. Garelli and A. Ferrero, "A unified theory for S-parameter uncertainty evaluation," *IEEE Trans. Microw. Theory Techn.*, vol. 60, no. 12, pp. 3844–3855, Dec. 2012.

[18] G. N. Phung and U. Arz, "Anomalies in multiline-TRL-corrected measurements of short CPW lines," in *Proc. 96th ARFTG Microw. Meas. Conf. (ARFTG)*, Jan. 2021, pp. 1–4.

[19] D. F. Williams, C. M. Wang, and U. Arz, "An optimal multiline TRL calibration algorithm," in *IEEE MTT-S Int. Microw. Symp. Dig.*, vol. 3, Jun. 2003, pp. 1819–1822.

[20] K. J. Silvonen, "A general approach to network analyzer calibration," *IEEE Trans. Microw. Theory Techn.*, vol. 40, no. 4, pp. 754–759, Apr. 1992.

[21] *170 GHz/220 GHz Broadband Vector Network Analysis Solution for on-Wafer Millimeter-Wave Component Characterization*, Keysight Technologies, and Virginia Diodes, D. M. Inc., and FormFactor, Keysight Technol., Santa Rosa, CA, USA, Tech. Rep., Jun. 2022.

[22] G. N. Phung, U. Arz, K. Kuhlmann, R. Doerner, and W. Heinrich, "Improved modeling of radiation effects in coplanar waveguides with finite ground width," in *Proc. 50th Eur. Microw. Conf. (EuMC)*, Jan. 2021, pp. 404–407.

[23] D. C. DeGroot, J. A. Jargon, and R. B. Marks, "Multiline TRL revealed," in *Proc. 60th ARFTG Conf. Dig. (Fall)*, Dec. 2002, pp. 131–155.

Robin Schmidt (Member, IEEE) received the M.Sc. degree in electrical engineering from L'Ecole Superieure d'Electricite, Rennes, France, in 2018, and the master's degree from Paris-Sud University, Orsay, France, in 2018. He is currently pursuing the Ph.D. degree at Katholieke Universiteit Leuven (KU Leuven), Leuven, Belgium.

Moved by his profound interest in applied physics, he has been searching to marry this passion with electronic design, which led him fast toward high-frequency electronics. Introduced to terahertz technologies within Paris-Sud University, his interests for the domain grew since a lot of fundamental research has to be followed in that domain, particularly related to metrology. Now employed as an Early Stage Researcher by Keysight Technology, Rotselaar, Belgium, his focus is the development of calibration structures for on wafer *S*-parameters' measurements in mm and submm-wave frequency.

Simone Clochiatti received the M.Sc. degree in electrical engineering from the Technical University of Denmark (DTU), Kongens Lyngby, Denmark, in 2018, with a focus on areas of RF, microwave engineering, and antennas. He is currently pursuing the Ph.D. degree in electrical engineering at the Department of Components for High-Frequency Electronics (BHE), University of Duisburg-Essen, Duisburg, Germany.

His research deals with the characterization of THz devices and integrated circuits for signal generation and detection, based on resonant tunneling diode (RTD) semiconductor device.

Enes Mutlu (Student Member, IEEE) was born in Essen, Germany. He received the M.S. degree in nanooptoelectronics from the University of Duisburg-Essen (UDE), Duisburg, Germany, in 2019, where he is currently pursuing the Ph.D. degree at the Department of High Frequency Electronic Devices.

His research work is based on the device development of resonant tunneling diodes and oscillator design at mm-waves. As a part of SFB/TRR 196, also called MARIE, he focuses on realizing efficient THz emitters with the future aim to investigate electronic beam steerable THz emitters.

Nils Weimann (Member, IEEE) received the Diploma degree in physics from the University of Stuttgart, Stuttgart, Germany, in 1996, and the Ph.D. degree in electrical engineering from Cornell University, Ithaca, NY, USA, in 1999.

He then worked as a member of Technical Staff with the Department of Solid-State Physics, Bell Laboratories, Murray Hill, NJ, USA. In 2012, he joined the Ferdinand-Braun-Institut (FBH), Berlin, Germany, leading the InP Devices Group. In 2017, he was appointed as a Full Professor with the University of Duisburg-Essen (UDE), Duisburg, Germany, chairing the Department of High Frequency Electronic Devices, Faculty of Engineering. Since 2019, he has been heading the UDE/FBH Joint Laboratory InP Devices. His research areas include high-frequency devices and circuits, in particular indium phosphide HBTs and resonant tunneling diodes, and nanowire structures for optoelectronic applications.

Prof. Weimann is a member of the MTT 2021 Terahertz Technology and Applications Committee.

Andrea Ferrero (Fellow, IEEE) received the Laurea and Ph.D. degrees in electronic from the Politecnico di Torino, Turin, Italy, in 1987 and 1992, respectively.

In 1992, he joined the Microwave Technology Division, Hewlett Packard, Santa Rosa, CA, USA, as a Visiting Scientist, and started his career at the Politecnico di Torino, as an Assistant Professor. In 1988, he worked with Aeritalia (Gruppo Sistemi Avionici), Turin, as a Microwave Measurement System Consultant on EMC problems for Avionics. In 2006, he became a Full Professor with the Politecnico di Torino, where he taught electronic instrumentation and measurements, and microwave instrumentation in the Electronic and Telecommunication Engineering Course until 2012. In 2013, he joined Agilent Technology (now, Keysight Technologies), Rotselaar, Belgium, as a Principal Research Engineer. Finally, he is a Competition Glider Pilot with more than 35 years of activity, 3000 flying hours on different gliders and small airplanes. He is the author or coauthor of over 100 articles on microwave technologies and measurements techniques. His current research interests are focused on device characterization, calibration techniques, VNA metrology, and signal recognition.

Prof. Ferrero became a member of the Technical Committee (MTT 2011) for microwave measurements in 2000 and the Chair of the same committee from 2017 to 2018. In 1994, he won the Canadian National Scientist Fellowship and spent one year at the Ecole Politechnic of Montreal, Montreal, QC, Canada. In 1994, he won the Microwave Best Presentation Award at 1994 MTT-S. In 1997, he won the Italian National Contest for Associate Professor Chair becoming an Associate Professor of the Politecnico di Torino for microwave measurements. In 2006, he won the IEEE Automatic Radio Frequency Techniques Group (ARFTG) Technology Award for advance in network analyzer calibration and non linear microwave measurement contributions. Since 1994, he has been an IEEE Reviewer of the Microwave Theory and Technique Society, and the Instrumentation and Measurement Society, and other international scientific journals. He has been an International Reviewer of the European Commission (EC) Metrology Program. He has served as a Reviewer for the Italian Ministry of Education and several other universities in Italy and abroad. Since 2017, he has been serving as an Associate Editor for the IEEE TRANSACTIONS ON MICROWAVE THEORY AND TECHNIQUES. He has been a Distinguished Microwave Lecture of the IEEE MTT Society.

Michael Dieudonné is currently the Director of Keysight Technologies, Rotselaar, Belgium. He is also the Department Manager of Keysight Laboratories and supervises research performed in different domains around 5G/6G, network test, and high-frequency metrology. He has been active in various international projects, such as the EURAMET EMPIR MET5G Project, coordinated European Union (EU) SAMURAI Project defining early day multiple input multiple output (MIMO) techniques for 4G systems, and European Union-Horizon 2020 (EU-H2020) Triangle (test of application in a 5G context). He currently works on test automation (OPentap.io), Open Radio Access Network (ORAN) test, the Internet of Things (IoT) test, 5G test, and 6G test.

Dominique M. M.-P. Schreurs (Fellow, IEEE) received the M.Sc. degree in electronic engineering and the Ph.D. degree from the University of Leuven (KU Leuven), Leuven, Belgium, in 1992 and 1997, respectively.

She has been a Visiting Scientist with Agilent Technologies, Santa Rosa, CA, USA; ETH Zürich, Zürich, Switzerland; and the National Institute of Standards and Technology, Boulder, CO, USA. She is currently a Full Professor with KU Leuven, where she is also the Chair of the Leuven Centre on Information and Communication Technology (Leuven ICT). Her current research interests include microwave and mm-wave characterization and modeling of transistors, nonlinear circuits, bioliquids; and system design for wireless communications and biomedical applications.

Prof. Schreurs served as the President for the IEEE Microwave Theory and Techniques Society from 2018 to 2019 and the Automatic Radio Frequency Techniques Group (ARFTG) Organization from 2018 to 2019. She is the TPC Co-Chair of International Microwave Symposium (IMS) 2023 and the General Chair of IEEE MTT-S International Microwave Biomedical Conference (IMBioC) 2023. She was the Editor-in-Chief of the IEEE TRANSACTIONS ON MICROWAVE THEORY AND TECHNIQUES. She was an IEEE MTT-S Distinguished Microwave Lecturer.